**Supplementary Information for**

# Atomic Mechanisms of Gold Nanoparticle Growth in Ionic Liquid by In Situ Scanning Transmission Electron Microscopy

Debora Keller*, Trond R. Henninen, Rolf Erni*

Electron Microscopy Center, Empa – Swiss Federal Laboratories for Materials Science and Technology, Überlandstrasse 129, CH-8600, Dübendorf, Switzerland

* Corresponding authors: Debora Keller (debora.keller@empa.ch) and Rolf Erni (rolf.erni@empa.ch)

**Table of Contents**

## 1. Depletion zones around larger particles

Fig. S1 shows an overview area of gold particles growing in ionic liquid. The field of view of 43 nm x 43 nm shows a large number of smaller particles (< 2 nm) and also three larger particles of 4.5 - 6.0 nm in diameter. The three larger particles are all surrounded by zones depleted of smaller particles of about 2.5 - 3.5 nm width. As such depletion zones were frequently observed in growing particle ensembles we assume that a considerable amount of the material consumed by the larger particles growing stems from smaller particles that are dissolved in the surrounding liquid. Therefore, we assume that Ostwald ripening contributes significantly to the particle growth.

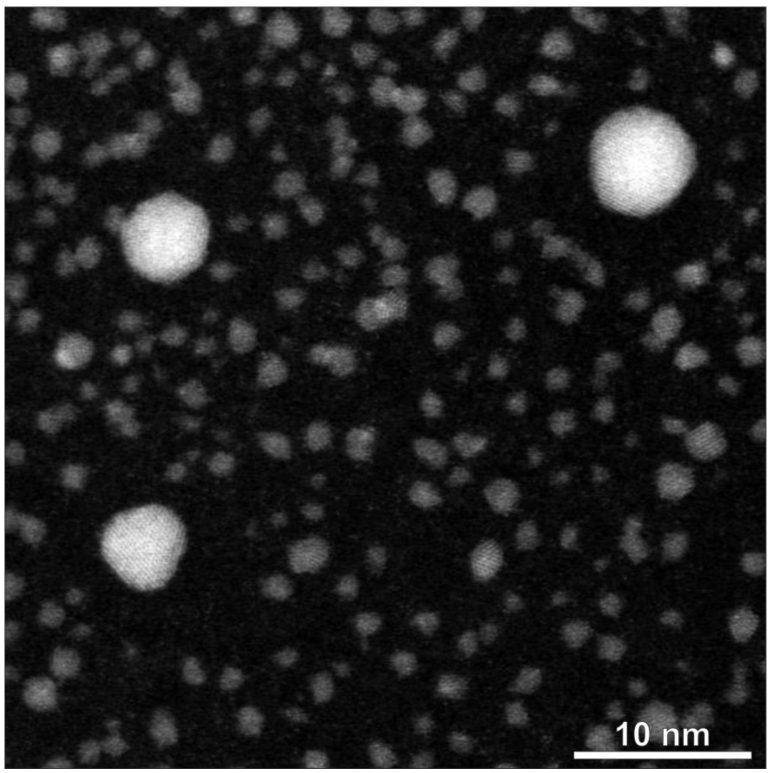


***Fig. S1.*** *Overview image of growing gold particles in the ionic liquid.*

## 2. Additional examples of rapid and slow coalescence processes

Fig. S2 shows an additional example of a rapid coalescence event which has however been induced by a large contact area. Two initially separated particles (0 s) build up a shared contact area (5 - 12 s), but they do not coalesce immediately after contact. Both particles continue rotating and restructuring for more than a minute. Then, the two particles coalesce by a sudden, rapid collapse of the smaller particle (81.5 -

82.0 s). Similarly as also observed in the process shown in Fig. 3a in the manuscript, a small protrusion is visible at the contact region shortly after the coalescence (82.5 s) until the particle finally relaxes to a more spherical shape (90 s).

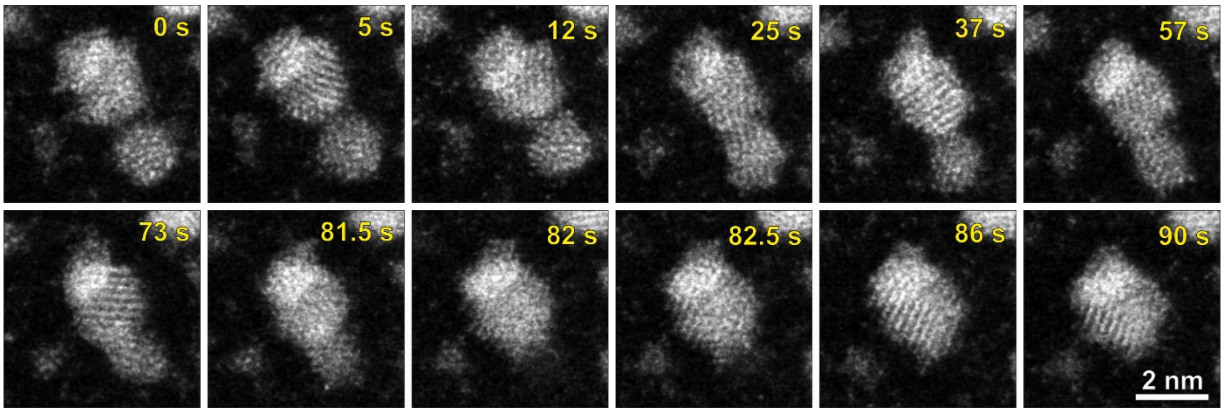


***Fig. S2.*** *Rapid coalescence event induced by a large contact area. After establishing a contact area (5 - 12 s) both particles remain stable for more than a minute before they merge by a sudden, rapid collapse of the smaller particle (81.5 - 82.0 s). The snapshots shown in this figure were extracted from Mov. S3d.*

In Fig. S3, two additional examples of slow coalescence through particle orientation and restructuring are shown: Fig. S3a shows the aggregation of initially four particles that align and fuse stepwise until a single, larger particle is obtained. Fig. S3b provides another example of two particles merging where it is clearly visible that both particles are reorienting and restructuring.

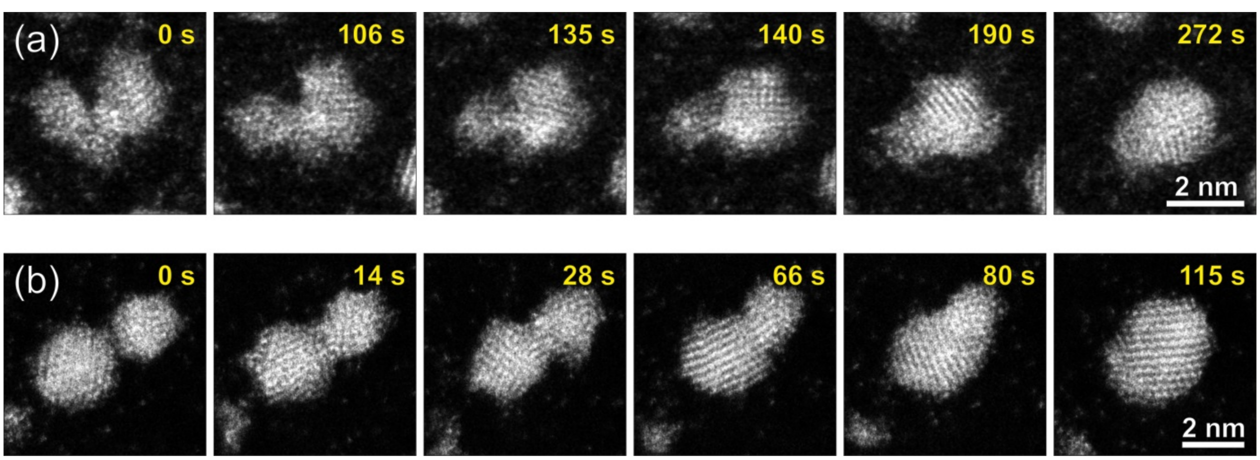


***Fig. S3:*** *Slow coalescence process. Coalescence examples of (a) four, and (b) two particles are shown that align, restructure and finally fuse into one crystal. The snapshots shown in Fig. S3a and S3b were extracted from Mov. S4b and S4c.*

## 3. Acquisition details for figures and movies

The detailed acquisition parameters applied for recording the time series are summarized in Tab. S1.

***Tab. S1.*** *Acquisition parameters used for the figures and the corresponding movies.*

| Figure | Movie | Dose rate [$e^{-}A^{-2}s^{-1}$] | Frame time [s] | *Displayed section of frames* | Pixel size [pm] |
|---|---|---|---|---|---|
| Fig. 1 | Mov. S1 (0-100 s)<br>Mov. S1 (101-300 s) | $0.6*10^4$<br>$2.5*10^4$ | 0.5<br>1 | *1-200* | 17.8<br>8.9 |
| Fig. 2a | Mov. S2a | $4.3*10^4$ | 0.5 | *90-190* | 12.6 |
| Fig. 2b | Mov. S2b | $2.2*10^4$ | 0.5 | *242-382* | 17.8 |
| Fig. 3a | Mov. S3a | $4.9*10^4$ | 0.5 | *1-50* | 12.6 |
| Fig. 3b | Mov. S3b | $2.2*10^4$ | 0.5 | *1-84* | 17.8 |
| Fig. 3c | Mov. S3c | $2.2*10^4$ | 0.25 | *170-290* | 6.3 |
| Fig. 4 | Mov. S4a | $2.1*10^4$ | 0.25 | *316-526* | 12.6 |
| Fig. S2 | Mov. S3d | $2.1*10^4$ | 0.25 | *177-677* | 12.6 |
| Fig. S3a | Mov. S4b | $2.1*10^4$ | 0.25 | *105-1194* | 12.6 |
| Fig. S3b | Mov. S4c | $8.5*10^4$ | 0.5 | *1116-1346* | 6.3 |

## 4. Beam damage and radiation effects

### a. Beam damage in [$Bu_4N$][Cl]

Direct observations of dynamic processes in liquid phase by (scanning) transmission electron microscopy ((S)TEM) require illumination of the sample by the electron beam. Interactions of the electron beam with the liquid, such as the formation of reactive radiation products and charging, are therefore present in any kind of liquid-phase (LP-)TEM experiment and cannot completely be excluded. Nevertheless beam effects can be minimized by choosing an appropriate liquid medium and can be controlled by monitoring the dose rates and total doses applied in an experiment.[1] The amount and the type of reactive species that are created in a liquid due to electron irradiation are determined by the stability of possible radiolysis products. The cations of ionic liquids typically react by a multitude less easily with solvated electrons than water, therefore, ionic liquids are much more beam resistant compared to aqueous solutions.[2] Especially ammonium-based ionic liquids, like [$Bu_4N$][Cl], show relatively high radiochemical stability amongst different ionic liquids and can stand much higher doses without significant damage as compared to aqueous solutions.[3-7] A detailed analysis of radiation damage in an imidazolium-based ionic liquid under similar irradiation conditions (STEM, dose rates ~10^4 $e^{-}$/Å$^2$s, duration of experiment 42 s) has previously been reported whereas no beam damage was observed in those experiments. In contrast, the experiments described in this work are performed with similar irradiation conditions and using a comparably more beam-resistant ionic liquid. Hence the beam damage is expected to be insignificant based on theoretical considerations. Experimentally, we can also confirm based on our observations, that no significant degradation of the ionic liquid and no solidification of the ionic liquid due to crosslinking by radicals is visible under the applied dose rates and total doses. As charging of the ionic liquid typically results in repulsion or accumulation of ionic liquid in the irradiated area, we can further assume that possible charging effects are also negligible in our experiments as long as no significant changes over time in the contrast, i.e. in the thickness of the ionic liquid film are recorded.

### b. Beam effects on gold atoms and particle growth processes

Due to the high beam resistance of the chosen ionic liquid, the irradiation creates a high number of solvated electrons and only few radiolyzed species of the ionic liquid. As a consequence, the electron beam is expected to create a reducing environment for gold ions in the ionic liquid, thus, indirectly affecting the particles by promoting growth. Further, the electron beam can directly impact the illuminated gold atoms by knock-on or displacement damage. However, the maximum energy that can be transferred from a 300 keV electron to a gold atom is about 4.3 eV[8,9] which is below the typical range for displacement energies of 10-50 eV (e.g. [9,10]). Therefore, we conclude that knock-on damage of gold atoms does not play a significant role in our experiments. Moreover, the 300 keV electron beam leads to less radiolysis products, due to the smaller inelastic cross section of 300 keV electrons compared to e.g. 200 keV electrons used in similar experiments[9], and thus should be beneficial for the chemical stability of the specimen.

## 5. Ionic liquid layer thickness estimation

For estimating the ionic liquid layer thickness we assume that the average atomic number (Z) of the carbon layer is similar to the average Z of the ionic liquid containing small amounts of gold. In this case, the thickness of an ionic liquid layer on a carbon film can be estimated by Eq. (1) where $T_{IL}$ is the thickness of the ionic liquid layer and $T_C$ is the thickness of the carbon film, which is about 20 nm. $Counts_{IL+C}$ is the average number of high-angle annular dark-field (HAADF) counts measured in an area where ionic liquid and carbon is present, $Counts_C$ is the average number of counts in an area where only carbon film is present and $Counts_V$ is the average number of counts in an area where the beam passes through vacuum.

Eq. S1 $$T_{IL} = T_C * \frac{Counts_{IL+C} - Counts_C}{Counts_C - Counts_V}$$

As an example, an overview image of a sample is shown in Fig. S4, from which the ionic liquid thickness was estimated to be 44 nm in thicker, isolated ionic liquid droplet and 20 nm in the thinner ionic liquid layer which is connected to a larger reservoir of ionic liquid.

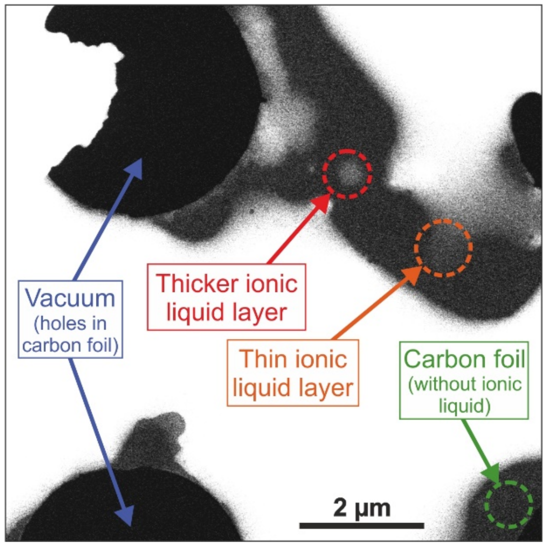


***Fig. S4:*** *Example of a HAADF overview image used for thickness estimations of ionic liquid layers according to Eq. S1. The average HAADF counts measured are: $Counts_V$ = 6600 in vacuum, $Counts_C$ = 12600 on the carbon film, $Counts_{IL+C}$ = 25700 on the thicker ionic liquid droplet and $Counts_{IL+C}$ = 18700 on the thin ionic liquid layer, thus resulting in estimated ionic liquid thicknesses of 44 nm and 20 nm, respectively.*

## 6. Supplementary movies

Mov. S1: Particle growth by attachment of single atoms observed at atomic resolution on a particle facet.

Mov. S2a: Example of a typical Ostwald ripening process.

Mov. S2b: Example of an Ostwald ripening process combined with mass transport by surface diffusion at a temporary particle contact area.

Mov. S3a: Rapid particle coalescence by jump-to-contact mechanism.

Mov. S3b: Rapid, bridge-induced particle coalescence.

Mov. S3c: Bridge-induced particle coalescence providing details about the local mass transport.

Mov. S3d: Rapid coalescence event induced by a large contact area.

Mov. S4a: Slow particle coalescence process.

Mov. S4b: Slow particle coalescence process of multiple particles.

Mov. S4c: Slow particle coalescence process.

## 7. References

1 T. J. Woehl and P. Abellan, *Journal of Microscopy*, 2017, **265**, 135–147.
2 J. F. Wishart, *J. Phys. Chem. Lett.*, 2010, **1**, 3225–3231.
3 T. Tsuda, S. Seino and S. Kuwabata, *Chem. Commun.*, 2009, **0**, 6792–6794.
4 E. M. Siedlecka, M. Czerwicka and S. S. and P. Stepnowski, *Curr. Org. Chem.*, 2011, **15**, 1974–1991.
5 É. Bossé, L. Berthon, N. Zorz, J. Monget, C. Berthon, I. Bisel, S. Legand and P. Moisy, *Dalton Trans.*, 2008, 924–931.
6 N. V. Ilawe, J. Fu, S. Ramanathan, B. M. Wong and J. Wu, *J. Phys. Chem. C*, 2016, **120**, 27757–27767.
7 J. F. Wishart and P. Neta, *J. Phys. Chem. B*, 2003, **107**, 7261–7267.
8 R. F. Egerton, in *Electron Energy-Loss Spectroscopy in the Electron Microscope*, ed. R. F. Egerton, Springer US, Boston, MA, 2011, pp. 111–229.
9 T. Miyata, F. Uesugi and T. Mizoguchi, *Sci. Adv.*, 2017, **3**, e1701546.
10 K. Nordlund, S. J. Zinkle, A. E. Sand, F. Granberg, R. S. Averback, R. E. Stoller, T. Suzudo, L. Malerba, F. Banhart, W. J. Weber, F. Willaime, S. L. Dudarev and D. Simeone, *Journal of Nuclear Materials*, 2018, **512**, 450–479.